

Long-Term X-Ray/UV Variability in ULXs

Norman Khan,^{1*} Matthew. J. Middleton,¹

¹*School of Physics & Astronomy, University of Southampton, Southampton, Southampton SO17 1BJ, UK*

Accepted XXX. Received YYY; in original form ZZZ

ABSTRACT

The focus of NASA’s *Swift* telescope has been transients and target-of-opportunity observing, resulting in many observations of ultraluminous X-ray sources (ULXs) over the last ~ 20 years. For the vast majority of these observations, simultaneous data has been obtained using both the X-ray telescope (XRT) and the ultraviolet and optical telescope (UVOT), providing a unique opportunity to study coupled variability between these bands. Using a sample of ~ 40 ULXs with numerous repeat observations, we extract stacked images to characterise the spatial extent of the UV-Optical emission and extract long-term light curves to search for first-order linear correlations between the UV and X-ray emission. We find that a small subset may show weakly correlated joint variability, while other sources appear to display non-linear relationships between the bands. We discuss these observations in the context of several theoretical models: precession, irradiation of the outer accretion disc and irradiation of the companion star. We conclude that more complicated analysis or higher quality data may be required to accurately constrain the nature of the joint X-ray and UV/optical emission in these sources.

Key words: stars: black holes – stars: neutron

1 INTRODUCTION

Ultraluminous X-ray sources (ULXs) are defined as off-nuclear, point-like sources with inferred isotropic luminosities exceeding $L > 10^{39} \text{ erg s}^{-1}$ (see the reviews of Roberts 2007; Kaaret et al. 2017; King et al. 2023). Pulsations unambiguously indicating the presence of neutron star (NS) accretors have been located in several ULXs (Bachetti et al. 2014; Fürst et al. 2016; Israel et al. 2017; Tsygankov et al. 2017; Doroshenko et al. 2018; Carpano et al. 2018; Sathyaprakash et al. 2019; Rodríguez Castillo et al. 2020) whilst the presence of a cyclotron resonant scattering feature in M51 ULX-8 (Brightman et al. 2018) and possible detection in NGC300 ULX1 (Walton et al. 2018b) also suggest the presence of neutron stars. Given the luminosities of these sources and the known accretor mass, it is inescapable that the accretion flow in such systems is super-critical, either in the flow or onto the star itself.

Should the Eddington limit be reached in the disc, then standard theory (i.e. Shakura & Sunyaev 1973; Poutanen et al. 2007) would predict powerful, mass-loaded winds which have been located in several ULXs to-date, both as imprints in the CCD spectra (Middleton et al. 2014, 2015b; Walton et al. 2016) and using higher energy-resolution detectors (Pinto et al. 2016, 2017; Kosec et al. 2018, 2021). A corollary of such accretion flows is that, providing the wind is optically thick, there should be some degree of collimation and the assumption of isotropy breaks down (King et al. 2001). The resulting spectrum (and timing properties) of a given ULX then depends on both the accretion rate and inclination of the source (Poutanen et al. 2007; Middleton et al. 2015a).

Should the accretion rate be high, we would naturally expect high

inclination ULXs to be dim in the X-rays and instead peak at lower frequencies (Poutanen et al. 2007). With emission from the wind photosphere being \sim Eddington, these may be prime candidates for detection by next-generation deep surveys (e.g. LSST: Middleton et al. in prep). A prime example of such an edge-on ULX is the Galactic source SS433 ($i = 78^\circ$), which, despite having an X-ray luminosity of only $\sim 10^{36} \text{ erg s}^{-1}$ appears to share many of the same characteristics of ULXs and is inferred to have considerably brighter, face-on X-ray luminosities (Cherepashchuk 2002; Fabrika 2004; Khabibullin & Sazonov 2016; Liu et al. 2015; Middleton et al. 2021) and emit at $\sim 10^{40} \text{ erg s}^{-1}$ in the UV (Dolan et al. 1997).

A change in the intrinsic X-ray/UV emission from a given ULX may be driven by either a change in mass accretion rate at larger radius or a change in our line-of-sight inclination to the inner-regions. The former may be the result of mass loss at large radii (Middleton et al. 2022), whilst the latter may be a result of disc warping due to irradiation (Pringle 1996; Pasham & Strohmayer 2013b) or precession of the super-critical disc and wind (Pasham & Strohmayer 2013a; Middleton et al. 2018, 2019b).

Whilst the intrinsic emission from high inclination ULXs may peak at low frequencies, in the optical/UV band there will also be emission from the secondary star which can be amplified if effectively irradiated, as well as emission from the outer disc (again, if effectively irradiated). Whilst there has been a great deal of study of ULXs in the optical – specifically to elucidate the nature of the companion star (Heida et al. 2014) – there has been limited exploration in the UV bands. However, it has been observed that in one ULX, the UV emission appears extremely bright ($> 10^{39} \text{ erg/s}$: Kaaret et al. 2017) and in the case of the PULX, NGC 7793 P13, an optical/UV super-orbital period is seen, out of phase with the X-ray super-orbital period (Fürst et al. 2016). Although not well explored, the correlation

* E-mail: nk7g14@soton.ac.uk

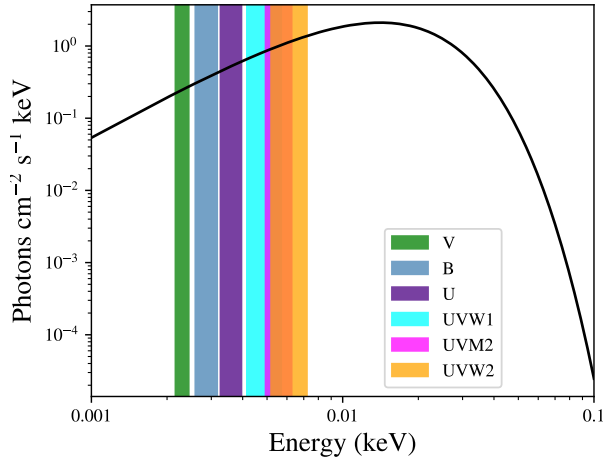


Figure 1. Black body spectrum (bbody in xspec) set at $kT = 0.005$ keV. Coloured are the effective energy ranges of the UVOT bands used for the flux calculation shown in figure 2.

between X-ray and low frequency emission should provide invaluable insight into the geometry and nature of the accretion flow. In this paper, we explore the general shapes of the X-ray/UV correlations we might expect for various scenarios and search for these within the Swift lightcurves of several prominent ULXs.

2 PREDICTIONS

In this section, we consider the theoretical impact on the coupled X-ray/UV properties of ULXs when ascribing the low frequency emission to various locations in the system. To simplify this picture we make the explicit assumption that ULXs which contain neutron stars all have dipole fields weak enough (or accretion rates high enough) that the classical super-critical picture of disc accretion (Poutanen et al. 2007) holds (i.e. that the magnetospheric radius, R_M , is much smaller than the spherisation radius, R_{sph}). Currently, measurements only exist for a handful of pulsating ULXs (see Walton et al. 2018b; Brightman et al. 2018; Middleton et al. 2019a; Fürst et al. 2023) but suggest field strengths of order $\sim 10^{11} - 10^{13}$ G which according to the canonical picture of PULXs should tend to lead to the condition that $R_M < R_{sph}$ (King & Lasota 2020).

2.1 Emission from the outer wind photosphere

Following the super-critical model of Poutanen et al. 2007, we assume that the wind photosphere extends out to some radius r_{out} and reprocesses the flux from the disc below the wind where the inflow starts to become locally super-critical, and some fraction of the radiation produced interior to r_{out} (the latter with a luminosity greater than or equal to the Eddington luminosity). A full understanding of the shape and intensity of the emergent SED requires full radiative magnetohydrodynamic (RMHD) simulations and extensive post-processing, which has not yet been performed in the case of ULXs (although see the work by Narayan et al. 2017 and Dai et al. 2018). In the absence of numerical studies, simple qualitative predictions are still possible. For a fixed inclination, increasing the mass accretion rate pushes r_{out} to a larger radius due to increased mass

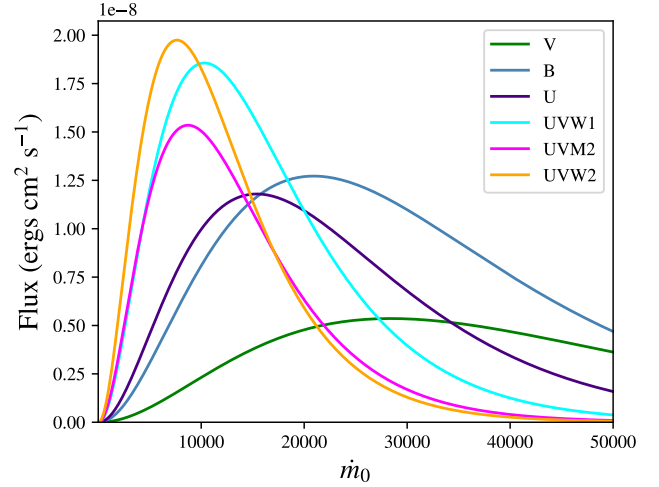


Figure 2. Flux in each of the UVOT bands as a function of the mass accretion rate \dot{m}_0 . The peak flux is reached at $\dot{m}_0 \sim 7000$ for the highest energy band (UVW2), much higher than is expected for ULXs; this means our UV view of high inclination ULXs, where the observed emission is from the wind photosphere, exists entirely within the region of UV emission on the left-hand side of the plot where the flux in a single band increases monotonically with \dot{m}_0 . The plot was made using the xspec model bbody with a normalized luminosity and a temperature set to T_{ph} (eq 1), $m = 1.4 M_\odot$, $\beta = \zeta = 1$, $f_{col} = 1.7$ and $\epsilon_w = 0.95$.

loading of the wind and the larger radial location of r_{sph} (Poutanen et al. 2007). Should the opening angle of the wind be connected to the accretion rate at large radius (as it would seem to be cf Jiang et al. 2014, 2019), then an increase in mass accretion rate will increasingly collimate the X-ray emission from within. What follows depends on the orientation of the observer. Should the observer be able to see into the wind cone, then the X-ray luminosity at all energies will increase, and the characteristic temperature associated with the spherization radius, T_{sph} will decrease. The expansion of the wind photosphere to larger radius will lead to a reduction in its temperature according to the formula of Poutanen et al. 2007 (eq 1):

$$T_{sph} \approx 0.8 f_{col} \left(\frac{\zeta \beta}{\epsilon_w} \right)^{1/2} m^{-1/4} \dot{m}_0^{-3/4} \text{ keV} \quad (1)$$

where f_{col} is a colour temperature correction factor, ζ , β and ϵ_w are constants relating to the wind-cone opening angle, outflow velocity and fractional energy content in powering the wind, m is the accretor mass in M_\odot , and \dot{m}_0 is the Eddington-scaled accretion rate.

By assuming the wind photosphere radiates as a blackbody at the characteristic temperature T_{sph} , that $\zeta \beta / \epsilon_w \approx 1$ (A simplification that can be made as all parameters can be considered of order unity), $f_{col} \approx 2$ (see Shimura & Takahara 1995), and accretor masses of $10 M_\odot$ and $1.4 M_\odot$, the UV emission in the highest energy band (UVW2) (taking the form of a blackbody, peaking around 3 kT) will increase in brightness until accretion rates in excess of $\dot{m}_0 \approx 5000 \times$ Eddington are reached for a $10 M_\odot$ black hole and $\dot{m}_0 \approx 7000 \times$ Eddington M_\odot for a $1.4 M_\odot$ neutron star (see figure 2). Such rates are safely above those inferred for known ULXs (Vasilopoulos et al. 2020). Below these limits, and for an orientation permitting a view into the wind-cone, one would expect a positive correlation between the X-rays and UV. It is conceivable that an observer could be oriented such that the closing of the wind cone inhibits their ability

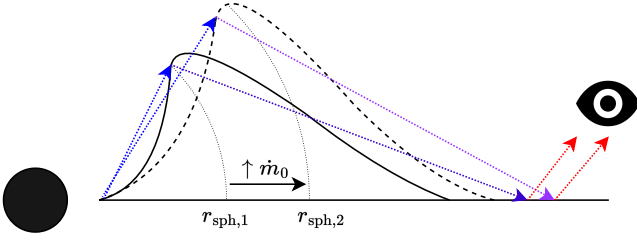


Figure 3. Schematic for the geometry of an irradiated outer disc, an increase in the mass accretion rate results in the spherization radius moving outwards and decreasing in temperature. High energy photons produced in the inner parts of the accretion flow are scattered by the large scale-height wind cone.

to see the collimated emission. In this case, there would be a change in the ratio between hard and soft X-ray emission (the soft being relatively more visible) accompanying a drop in T_{sph} . This would result in an anti-correlation between T_{sph} and the UV brightness and a more complex correlation with spectral hardness.

For a fixed accretion rate, a change in the inclination of the disc/wind, driven by precession (e.g. Middleton et al. 2018, 2019b) would result in changes to the X-ray spectral colours similar to the case of the wind-cone closing (see Middleton et al. 2015b). In short, when the cone precesses to higher inclinations to our line-of-sight, the X-ray emission should diminish, and the low frequency emission should become brighter, leading to an anti-correlation between the X-ray and UV emission (assuming the accretion rate is high enough for the wind photosphere to emit substantially at such low energies).

2.2 Irradiated outer disc

It has been suggested that the outer accretion disc could be irradiated by X-ray emission from the inner regions after scattering by the wind (Sutton et al. 2013). As long as this irradiating SED has sufficient intensity above 2 keV, down-scattering of these photons can produce a UV-shoulder (Gierliński et al. 2008). Exploring irradiation requires RMHD simulations and radiative transfer calculations to follow the photons from the inner regions to the outer disc. However, such calculations have yet to be performed, and so we instead base our reasoning on a simplified picture (see figure 3).

Should the accretor be a black hole or a low dipole field neutron star ($\lesssim 10^9 G$), then the spectrum from the innermost regions is insensitive to accretion rate (Poutanen et al. 2007) due to mass loss at larger radii. If the ULX contains a high dipole field-strength neutron star (up to $\sim 10^{13} G$), the emergent spectrum above 2 keV is predicted to be dominated by emission from the accretion column, with photons scattering to escape the magnetosphere (Mushtukov et al. 2017). Assuming the magnetospheric radius lies within r_{sph} , then the accretion rate through the magnetosphere is mostly insensitive to the accretion rate at larger radii (see e.g. King & Lasota 2020 although see also Chashkina et al. 2019). Assuming the intrinsic spectrum from the accretion column above 2 keV (see Brightman et al. 2016; Walton et al. 2018a) does not change, we need only consider the changes in the scattering medium between the outer disc and inner regions. As the accretion rate at large radius increases, the wind cone closes and the optical depth of the wind increases (see figure 3). There are then more scatterings within the wind cone, which reduces the energy of photons created in the inner regions; any escaping photons are therefore likely to be at lower energy and less likely to thermalise in

Prediction	\dot{m}	Inclination	Flux	
			X-ray	UV
Wind Photosphere	Low	Low (face-on)	■	■
Wind Photosphere	Low	Intermediate	■	■
Wind Photosphere	Low	High (Edge-on)		■
Wind Photosphere	High	Low (face-on)	■	■
Wind Photosphere	High	Intermediate	■	■
Wind Photosphere	High	High (Edge-on)		■
Irradiated outer disc	Low	Low (face-on)	■	■
Irradiated outer disc	Low	Intermediate	■	■
Irradiated outer disc	Low	High (Edge-on)		■
Irradiated outer disc	High	Low (face-on)	■	■
Irradiated outer disc	High	Intermediate	■	■
Irradiated outer disc	High	High (Edge-on)		■

Table 1. Predictions of the relative X-ray to UV emission originating from the wind photosphere and irradiation of the outer disc. The blue and red bars provide a visual representation of the relative observed intensity of the emitted radiation in the X-ray and UV bands. These estimates are approximate and quantized to four discrete lengths to serve as a qualitative indicator.

the outer disc (Gierliński et al. 2008). The converse is true for a drop in accretion rate.

For a fixed observer inclination but a varying accretion rate, the presence (or lack of) a correlation between the X-rays and UV resulting from an irradiated outer disc once again depends on whether an observer can see into the wind cone. Should an observer be able to view the innermost regions directly, then an increase in accretion rate will lead to an increase in X-ray flux (and decrease in T_{sph}) and a drop in UV flux, as fewer hard X-rays impinge on the outer disc. Should an observer instead view the inner flow at higher inclinations, then a more complex change in spectral hardness will result (as described in Middleton et al. 2015b). For a fixed accretion rate, a change in inclination of the inner disc and wind will not change the UV emission (even if the wind were to tilt away from us, it would still irradiate the far side of the disc) and the UV and X-rays will be uncorrelated.

2.3 Irradiated companion star

A third option, distinct from the above two – and proposed to explain the anti-phase optical super-orbital period seen in NGC 7793 P13 (Fürst et al. 2021) – is that the X-ray cone sweeps over the companion star and hard X-rays thermalise in the outer layers of the star leading to enhanced low frequency emission (Motch et al. 2014). To explore this scenario, we simulate a cone of X-ray emission irradiating a star at different orbital phases and different orientations relative to each other and the observer. Figure 4 shows a schematic of how the irradiated area (shown in light blue) from a cone of X-ray emission may vary as it sweeps over the star. The irradiated projected area seen by an observer is subject to many variables, including the size and shape of the orbit, star and cone, as well as the position of the observer. For further elaboration on the specific implementations of the irradiated companion model, please refer to Appendix A.

Figure 5 shows how the irradiated fraction, defined as the projected area seen by the observer divided by the maximum possible projected area $A_{\text{proj}}/\pi R_{\star}^2$, varies as a function of the (circular) orbital phase.

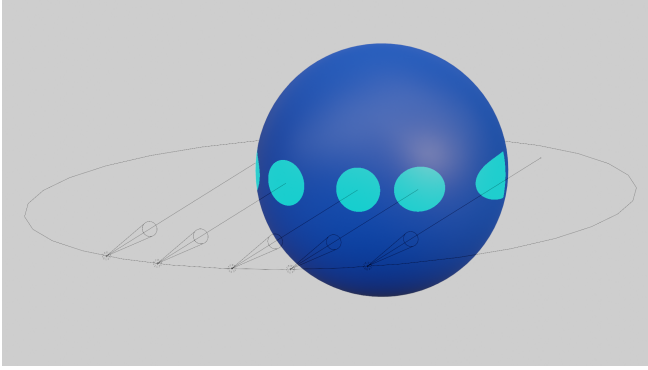


Figure 4. Schematic of irradiation of the secondary star as a tight cone of X-ray emission travelling on an elliptical orbit.

The transit is simulated for a cone sweeping directly through the centre of the star and is shown for three different observer inclinations. It is worth noting that the inclination parameter alone is not sufficient to fully describe the configuration of the system and the resulting irradiated area, this is as the entire system can be rotated while the inclination remains unchanged resulting in different projected areas for the same inclination value. Never the less, for illustrative purposes figure 5 shows how the profile of a transit may be significantly altered by the observer’s position.

If we were to assume that the axis of the wind-cone is perpendicular to the orbital axis, only wind-cone half-opening angle ($\theta/2$) which satisfy $\theta/2 > \arccos(R_\star/a)$ would be able to irradiate the star (where R_\star is the radius of the companion star and a is the average semi-major axis of the orbit). For example, a half-opening angle of 10° would require a $R_\star/a \approx 1$ which poses issues for stable accretion. Allowing for larger opening angles will of course lower the value of the ratio of R_\star/a although, as super-critical accretion demands a half-opening angle of at least 45° (where the scale-height of the disc is approximately unity), this requires $R_\star/a > 0.7$. Thus, large amounts of irradiation likely require an offset between the axis of the wind cone and that of the orbit (which may naturally lead to precession of the wind cone itself [Middleton et al. 2018, 2019b](#)).

Estimates for the eccentricity of ULX orbits have been obtained for a few pulsating sources, where the pulse arrival time allows for the modelling of the orbital parameters of the system. Based on modelling of the X-ray pulsations in NGC 7793 P13, ([Fürst et al. 2018](#)) find an eccentricity of $e \leq 0.15$, whilst ([Bachetti et al. 2014](#)) found that M82 X-2 had a near circular orbit of $e = 0.003$. In the absence of any detailed orbital information, we therefore assume a simple circular orbit in our model.

We have investigated the potential impact of an irradiated companion, illuminated by a cone of X-ray emission, on the observed UV/optical emission in ULXs. Our model is subject to limitations and uncertainties, and it is possible that specific conditions may be required for its geometry to be a reality in these sources. However, despite these challenges, it may be possible in the future to determine the ephemeris based on the observed profiles seen in the UV/optical light curves of these sources. High-resolution spectroscopy can also be used to determine whether significant heating of the star’s outer layers is present from specific spectral lines. In the next section, we will describe our approach to obtaining observations and reducing data to create long-term light curves for a sample of ULXs.

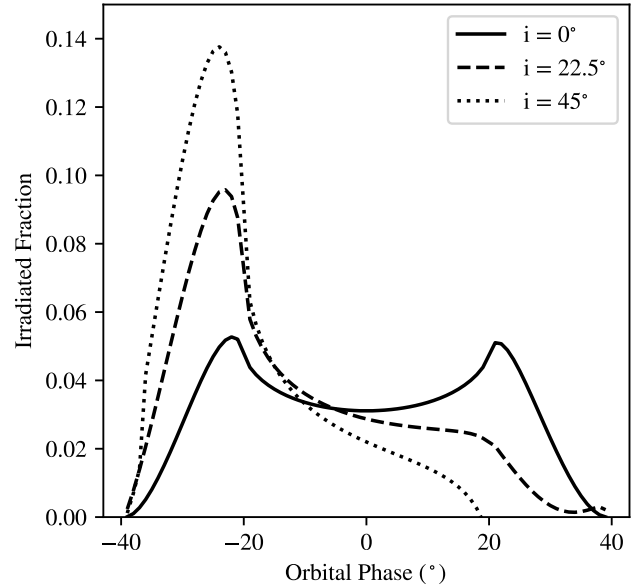


Figure 5. How the irradiated fraction, defined as $A_{\text{proj}}/\pi R_\star^2$, varies as a function of orbital phase transiting through a cone of emission with opening angle $\theta = 20^\circ$. The transit is shown for three different observer inclinations, $i = 0, 22.5$ and 45 degrees. A ratio of $R_\star/a = 0.5$ is assumed.

3 OBSERVATIONS AND DATA REDUCTION

The Neil Gehrels Swift Observatory (*Swift*) ([Gehrels et al. 2004](#)) is capable of observing simultaneously in both the UV and X-ray bands via its UVOT ([Roming et al. 2005](#)) and XRT ([Burrows et al. 2005](#)) cameras, and so provides a unique opportunity to explore whether observations of ULXs are consistent with any of the predictions discussed above. We begin by creating our ULX sample by crossmatching several ULX catalogues, ([Earnshaw et al. 2019](#); [Kovlakas et al. 2020](#); [Bernadich et al. 2022](#); [Walton et al. 2022](#)) with the *Swift* Master Catalogue (SWIFTMASSTR), accessible via HEASARC¹. For the sake of comparison to nearby sources where data quality is high, we also include three extensively studied Galactic sources which reach super-Eddington rates of accretion, Swift J0243.6+6124, SS433 and V404 Cygni. Swift J0243.6+6124 is known to contain a magnetised neutron star and appear as a ULX ([van den Eijnden et al. 2020](#)), SS433 is widely considered to be an edge-on ULX ([Fabrika 2004](#); [Middleton et al. 2021](#)) and V404 Cygni is a LMXB which reached around or just in excess of its Eddington luminosity during its 2015 outburst ([Motta et al. 2017](#)).

We locate all observations where the source lies within the nominal ($23.6'$) XRT field-of-view. Due to the differences between the XRT and UVOT field-of-view, there is a mismatch between the number of observations in both bands. We set the requirement that there be 20 observations in both bands for a source to appear in our sample. For each source, we manually cross-matched with SIMBAD to obtain distances and positions. The final sample with relevant information is shown in Table 2.

¹ <https://heasarc.gsfc.nasa.gov>

Source Name	RA "h:m:s"	DEC "d:m:s"	λ	Position reference	D Mpc	D meth.	D reference	UV Emis.
V404 Cygni	20 24 03.8254	+33 52 01.962	O	Gaia Collaboration (2018)	0.0023	parallax	Miller-Jones et al. (2009)	PL
Swift J0243.6+6124	02 43 40.4252	+61 26 03.757	O	Gaia Collaboration (2020)	0.0055	parallax	Gaia Collaboration (2020)	PL
SS433	19 11 49.5647	+04 58 57.827	O	Gaia Collaboration (2020)	0.0055		Blundell & Bowler (2004)	PL
SMC X-3	00 52 05.6251	-72 26 04.228	O	Gaia Collaboration (2020)	0.0600	cepheid	Karachentsev et al. (2017)	PL
IC10 X-1	00 20 29.09	+59 16 51.9	X	Bauer & Brandt (2004)	0.7943	redshift	Lianou et al. (2019)	N
M31 ULX-1	00 42 53.15	+41 14 22.9	X	Kaur et al. (2012)	0.8200	T-RDB	Karachentsev et al. (2017)	N
M33 ULX-1	01 33 50.8965	+30 39 36.630	O	Gaia Collaboration (2020)	0.9300	T-RDB	Karachentsev et al. (2017)	PL
NGC300 ULX-1	00 55 04.86	-37 41 43.7	O	Barbon et al. (2008)	2.0230	redshift	Lianou et al. (2019)	PL
NGC55 ULX	00 15 28.89	-39 13 18.8	X	Lin et al. (2012)	2.1100	T-RDB	Karachentsev et al. (2017)	Edg
IC342 ULX-1	03 45 55.612	+68 04 55.29	O	Feng & Kaaret (2008)	3.4356	redshift	Lianou et al. (2019)	N
IC342 ULX-2	03 46 15.61	+68 11 12.8	X	Heida et al. (2014)	3.4356	redshift	Lianou et al. (2019)	N
NGC4945 XMM-1	13 05 32.89	-49 27 34.1	X	Swartz et al. (2004)	3.4674	redshift	Lianou et al. (2019)	E
Holmberg II X-1	08 19 28.99	+70 42 19.4	X	Heida et al. (2014)	3.4674	redshift	Lianou et al. (2019)	E
M81 X-6	09 55 32.95	+69 00 33.6	X	Heida et al. (2014)	3.5975	redshift	Lianou et al. (2019)	E
M82 X-2	09 55 51.040	+69 40 45.49	X	Kaaret et al. (2006)	3.6141	redshift	Lianou et al. (2019)	E
NGC253 X-2	00 47 32.97	-25 17 50.2	X	Liu & Bregman (2005)	3.6983	redshift	Lianou et al. (2019)	E
NGC253 X-9	00 47 22.59	-25 20 50.9	X	Heida et al. (2014)	3.6983	redshift	Lianou et al. (2019)	N
NGC247 ULX-1	00 47 04.00	-20 47 45.7	X	Liu & Bregman (2005)	3.7200	T-RDB	Karachentsev et al. (2017)	N
NGC7793 P13	23 57 50.90	-32 37 26.6	X	Pannuti et al. (2011)	3.7325	redshift	Lianou et al. (2019)	PL
Holmberg IX X-1	09 57 53.290	+69 03 48.20	O	Abazajian et al. (2009)	3.8500	T-RDB	Karachentsev et al. (2017)	E
NGC1313 X-1	03 18 20.00	-66 29 10.9	X	Heida et al. (2014)	4.2500		Tully et al. (2016)	N
NGC1313 X-2	03 18 22.00	-66 36 04.3	X	Liu & Bregman (2005)	4.2500		Tully et al. (2016)	E
NGC5204 ULX-1	13 29 38.62	+58 25 05.6	X	Heida et al. (2014)	4.5900	T-RDB	Karachentsev et al. (2017)	E
UGC6456 ULX	11 28 03.000	+78 59 53.41	O	Vinokurov et al. (2020)	4.6300	T-RDB	Karachentsev et al. (2017)	E
NGC4395 ULX-1	12 26 01.53	+33 31 30.6	X	Heida et al. (2014)	4.7600		Tully et al. (2016)	E
M83 ULX-1	13 37 05.13	-29 52 07.1	X	Long et al. (2014)	4.8978	redshift	Lianou et al. (2019)	N
M83 ULX-2	13 37 20.12	-29 53 47.7	X	Liu & Bregman (2005)	4.8978	redshift	Lianou et al. (2019)	E
NGC5408 ULX-1	14 03 19.63	-41 22 58.7	X	Heida et al. (2014)	5.3211	redshift	Lianou et al. (2019)	N
NGC6946 ULX-1	20 35 00.11	+60 09 08.5	X	Lin et al. (2012)	6.7298	redshift	Lianou et al. (2019)	E
NGC6946 ULX-3	20 35 00.74	+60 11 30.6	X	Swartz et al. (2004)	6.7298	redshift	Lianou et al. (2019)	PL
M101 ULX-1	14 03 32.38	+54 21 03.0	X	Heida et al. (2014)	7.1121	redshift	Lianou et al. (2019)	N
NGC4559 ULX-1	12 35 51.71	+27 56 04.1	X	Heida et al. (2014)	7.1450	redshift	Lianou et al. (2019)	E
M51 ULX-7	13 30 01.01	+47 13 43.9	X	Heida et al. (2014)	7.6000	redshift	Cappellari et al. (2011)	E
NGC5585 ULX	14 19 39.39	+56 41 37.8	X	Heida et al. (2014)	7.8300		Tully et al. (2016)	PL
NGC925 ULX-1	02 27 27.53	+33 34 42.9	X	Heida et al. (2014)	9.2045	redshift	Lianou et al. (2019)	E
NGC925 ULX-2	02 27 21.52	+33 35 00.8	X	Heida et al. (2014)	9.2045	redshift	Lianou et al. (2019)	E
NGC7090 ULX-3	21 36 31.94	-54 33 57.2	X	Lin et al. (2012)	9.5060	redshift	Lianou et al. (2019)	Edg
NGC5907 ULX	15 15 58.60	+56 18 10.0	X	Swartz et al. (2011)	17.2187	redshift	Lianou et al. (2019)	Edg
NGC1365 X-1	03 33 34.60	-36 09 35.0	X	Liu & Bregman (2005)	17.2982	redshift	Lianou et al. (2019)	N
NGC1365 X-2	03 33 41.85	-36 07 31.4	X/O	Strateva & Komossa (2009)	17.2982	redshift	Lianou et al. (2019)	PL
NGC1042 ULX-1	02 40 25.62	-08 24 28.9	X	Lin et al. (2012)	19.2000		Oey et al. (2007)	N
ESO 243-49 HLX-1	01 10 28.30	-46 04 22.3	X	Webb et al. (2010)	115.3500		Tully et al. (2016)	N

Table 2. Source information for those ULXs investigated in this paper, sorted by host galaxy distance. λ corresponds to the wavelength (X-ray or optical) that the position was acquired in. The ‘D meth.’ column denotes the method used for determining the distance (where T-RDB is Tip of the red-giant branch). The ‘UV Emis.’ column corresponds to the spatial extent of the UV/optical emission based on visual inspection of the stacked UVOT images.

3.1 XRT Data Reduction

XRT data was extracted using the standard *Swift*/XRT processing pipeline (Evans et al. 2009), using the SIMBAD coordinates of the source, and the ‘simple’ centroid method with a positional error of 1" (see Evans et al. 2009). We extract light curves in three bands, full (0.3 – 10.0 keV), soft (0.3 – 1.5keV) and hard (1.5 – 10.0keV), with the time binning set at a single point per observation. Using the full band data, we set the minimum source significance – defined as the number of counts in the source region divided by the square root of the counts in the source and background ($C_{\text{src}}/\sqrt{C_{\text{src}} + C_{\text{bkg}}}$) – to the default value of 3; observations where the source is not detected at or above this threshold yield upper limits. The pipeline additionally calculates the hardness ratio, defined as the ratio of hard to soft count rates $HR = C_{\text{hard}}/C_{\text{soft}}$. 1σ errors are provided for each

of the above measurements. The pipeline also includes GOOD and BAD values, which indicates whether the pipeline was able to obtain a centroid in a given snapshot, (such that BAD values are potentially unreliable).

3.2 UVOT Data Reduction

UVOT data were processed locally using HEASARC v6.29 and the November 8, 2021 CALDB. We stacked all UVOT and XRT observations, combining them into a single image and manually inspected to identify any clear counterparts.

For each source, a circular extraction region with a radius of 5" was centred on the Swift XRT position, while background regions were manually positioned in a contaminant-free location with a size

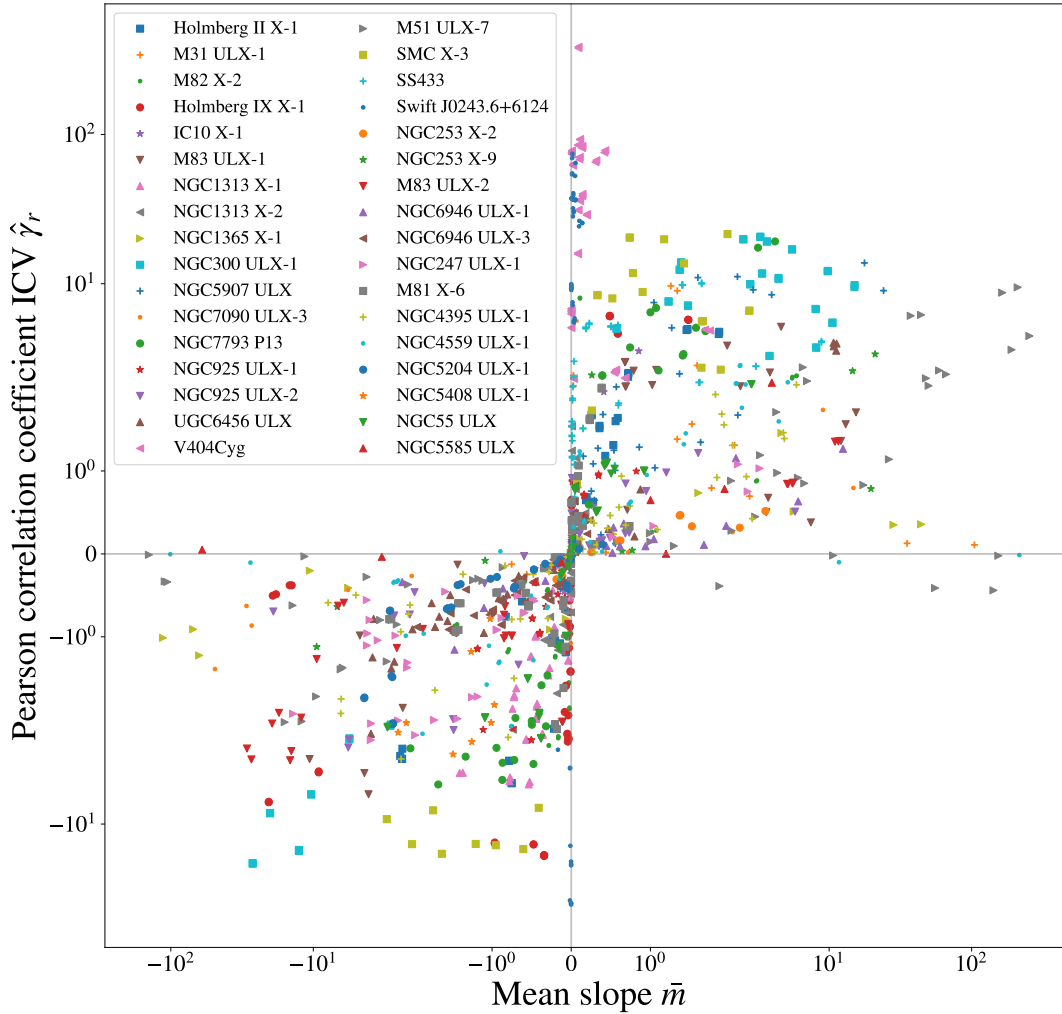


Figure 6. Mean slope \bar{m} (x) plotted against the inverse coefficient of variation of the Pearson correlation coefficient $\hat{\gamma}_r$ for all simulations.

of 15" as recommended by the UVOT data analysis manual². The distances between the centres of the UVOT and XRT (SIMBAD) source regions as well as the position of the UVOT background regions are provided in the supplementary material.

Level 2 UVOT images were processed locally using the `uvotimsum` to combine all snapshot extensions, then `uvotsource` with a signal-to-noise threshold of 3 was used to obtain photometric magnitudes in a given observation. We then determined whether the source was detected using the `NSIGMA` column provided as output from `uvotsource`. All observations of a given source were combined to produce a long term light-curve in all of the UVOT bands: V (5469 Å), B (4392 Å), U (3465 Å), UVW1 (2600 Å), UVM2 (2246 Å), UVW2 (1928 Å).

4 ANALYSIS AND RESULTS

4.1 UV Counterparts

The ‘UV Emis.’ column in Table 2 indicates the spatial nature of the UV emission of the source based upon the stacked images. Sources

with point-like UV counterparts and emission regions comparable to *Swift*’s PSF are labelled as ‘PL’, sources in or near regions of extended UV emission as ‘E’, those that do not display strong UV emission in the images are labelled as ‘N’, and three in edge-on galaxies ‘Edg’ where point-sources in the UV/optical are difficult to disentangle from the galactic emission.

4.2 Testing for linear X-ray/UV correlations

A cut of $\pm 5\sigma$ around the mean count rate was applied to both the UVOT and XRT data prior to simulating. This cut resulted in only 5 observations being excluded due to UVOT outliers, which were due to observations where the source was close to the edge of the detector or the background region was located within the fits image but outside the detector plate. Around ~ 30 observations were excluded due to XRT outliers, some of these are instrumental however others may be real and be due to source flaring, we find that around 0-3 observations are excluded for each lightcurve that may be composed of several hundred data points, the removal of these outliers results in marginally weaker detected correlations meaning that our results constitute a slightly more conservative estimate. To search for linear correlations in the clean X-ray and UVOT light curves, we employ the following method: for each observation data point we sampled

² https://swift.gsfc.nasa.gov/analysis/UVOT_swgguide_v2_2.pdf

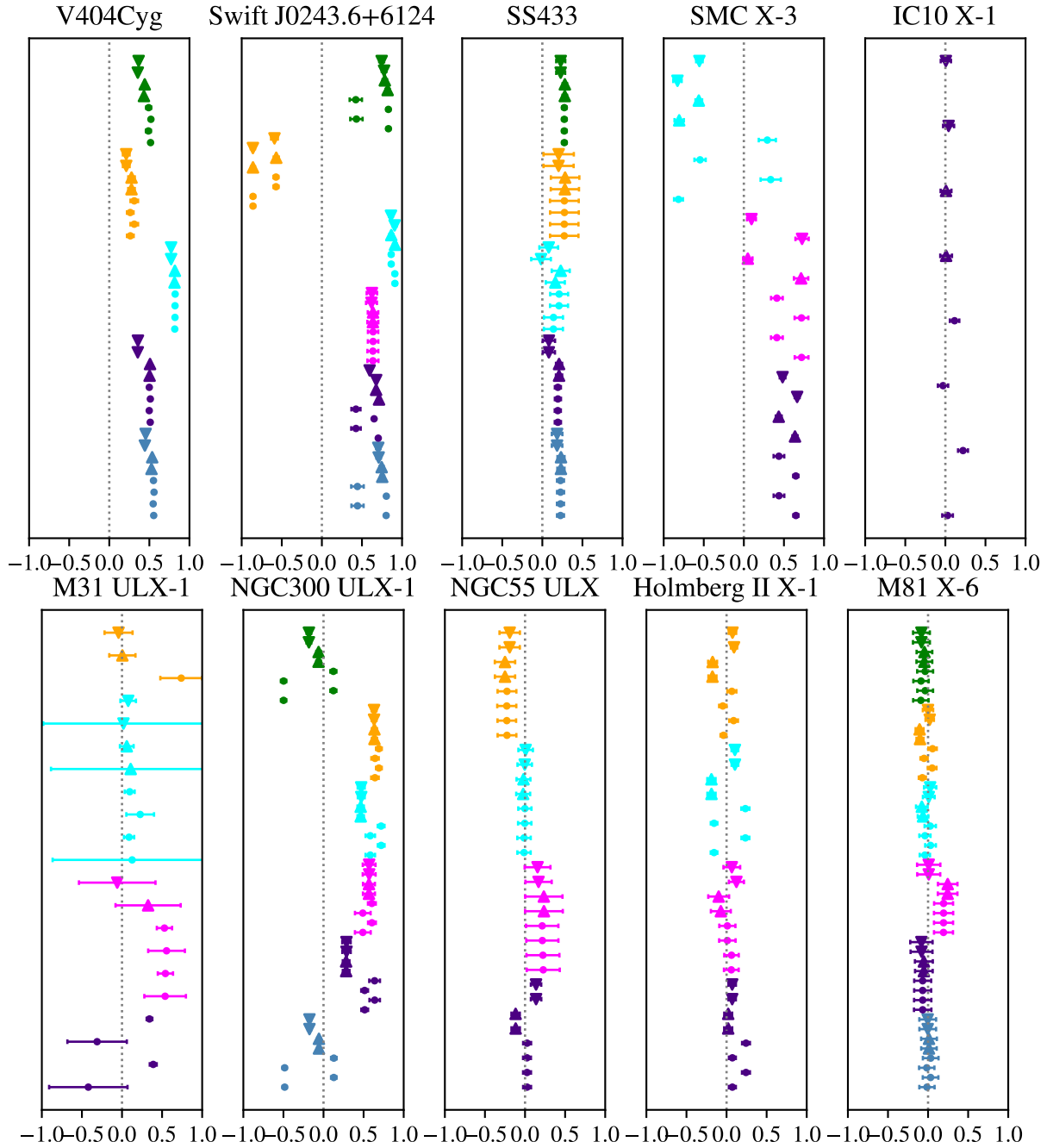


Figure 7. Distribution of the correlation coefficient for 10 of the sources investigated. Error bars correspond to 1σ , calculated from 10,000 Monte Carlo iterations. Colours correspond to the different UVOT filters used (See legend in figures 1 & 2) and are displayed in decreasing energy from top to bottom. The marker on the datapoint denotes which of the three XRT band with which the correlation was carried out with: The full band is denoted with a dot (\bullet), the hard band by an upwards triangle (\blacktriangle) and the soft band with a downwards triangle (\blacktriangledown), the correlations against the hardness ratio are not shown here. The same colour and marker may appear multiple times as separate simulations were conducted with the inclusion or exclusion of upper limits and/or bad data points.

the 1σ error on the count rate in both the XRT and UVOT bands assuming Gaussian distributions; if the observation contained an upper limit, the data point was sampled assuming a uniform distribution between 0 and this value. This sampling allows us to obtain realisations of the light curve with the same time-sampling as the original. We then performed a least-squares fit with a straight line of the form $y = mx + c$ to the re-sampled data points and calculated the Pearson correlation coefficient r given by:

$$r = \frac{\sum_{i=1}^n (x_i - \bar{x})(y_i - \bar{y})}{\sqrt{\sum_{i=1}^n (x_i - \bar{x})^2} \sqrt{\sum_{i=1}^n (y_i - \bar{y})^2}} \quad (2)$$

where x_i and y_i are the i th values in the sample, while \bar{x} and \bar{y} are the means over all the n data points. This resampling and fitting process was repeated 10,000 times to obtain posterior distributions for r , m and c , from which the mean and standard deviation were calculated.

To assess how well constrained are the posterior distributions for

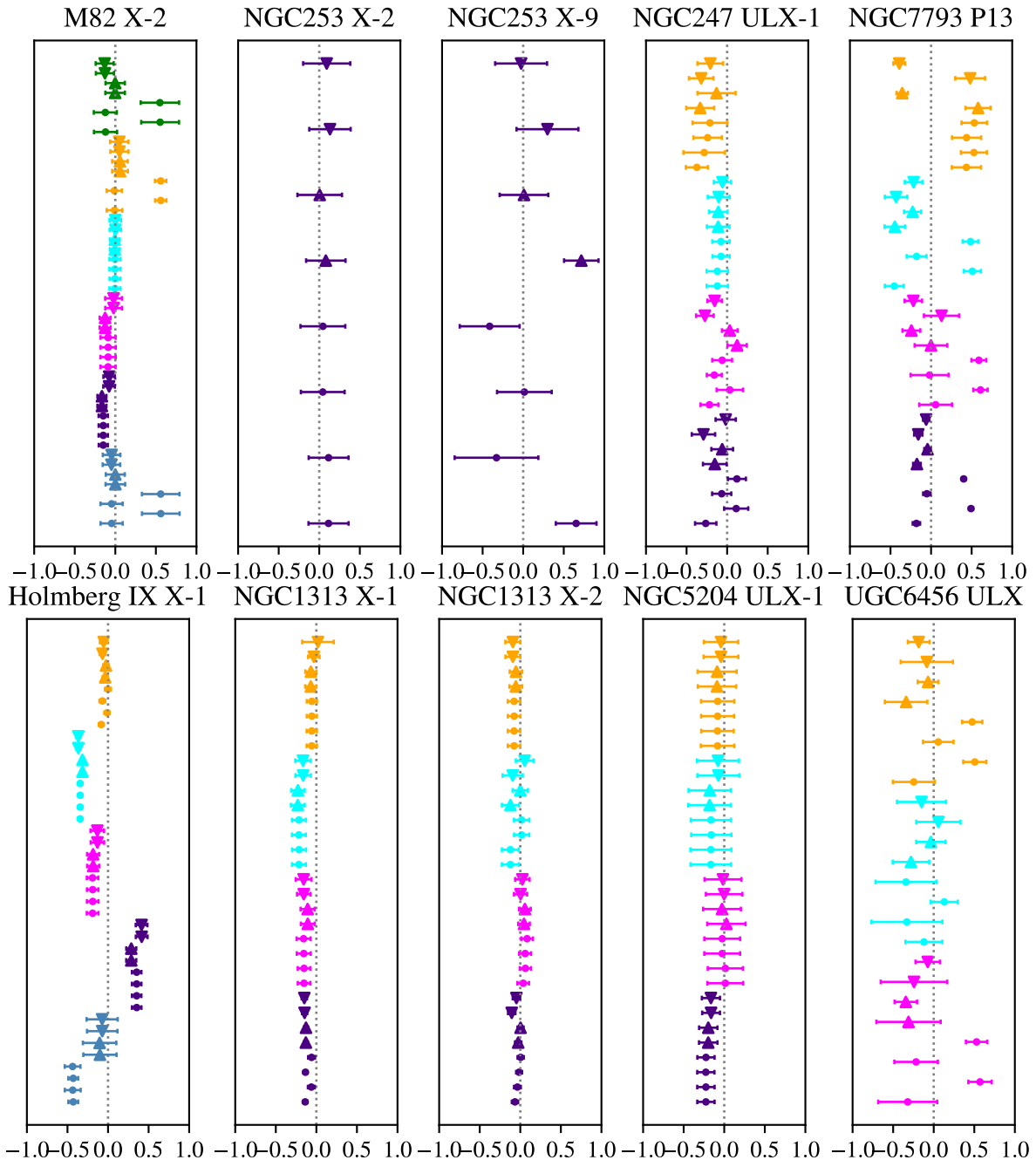


Figure 8. See caption for figure 7.

the fit parameters, we calculate the inverse coefficient of variation (ICV) ($\hat{\gamma}_{\text{par}}$) by dividing the mean of the fit parameters ($\overline{\text{par}}$) by their standard deviation (σ_{par}), i.e. $\hat{\gamma}_{\text{par}} = \overline{\text{par}}/\sigma_{\text{par}}$. The absolute value of $\hat{\gamma}_{\text{par}}$ may be interpreted as a significance value, with higher values corresponding to more strongly peaked distributions (i.e. the distribution has less scatter).

Simulations were carried out on all possible combinations of the four X-ray bands (full, soft, hard, HR), and the six UVOT filters. Simulations were additionally carried out including and excluding observations labelled as BAD in the XRT pipeline, as well as data points labelled as upper limits in the full XRT band. The simulation grid implies that a single source may have a total of 24 possible simulation combinations for the full XRT band, and 36 for the

remaining XRT bands (hard, soft and HR), giving a maximum of 60 correlations per source, assuming that the source has been visited in all UVOT bands and its XRT light curves contain both BAD and upper limit data points. In practice this is not the case and the total number of sets of simulations for each source is almost always lower than 60.

Figure 6 shows the mean value of the slope (m) and the ICV of the Pearson correlation coefficient ($\hat{\gamma}_r$) across all of our simulations. Sources appear multiple times on the plot due to the aforementioned grid in simulation space. The diagonal distance from the centre in this parameter space might provide an indication that a correlation exists – the upper right corresponding to positive correlations, the lower

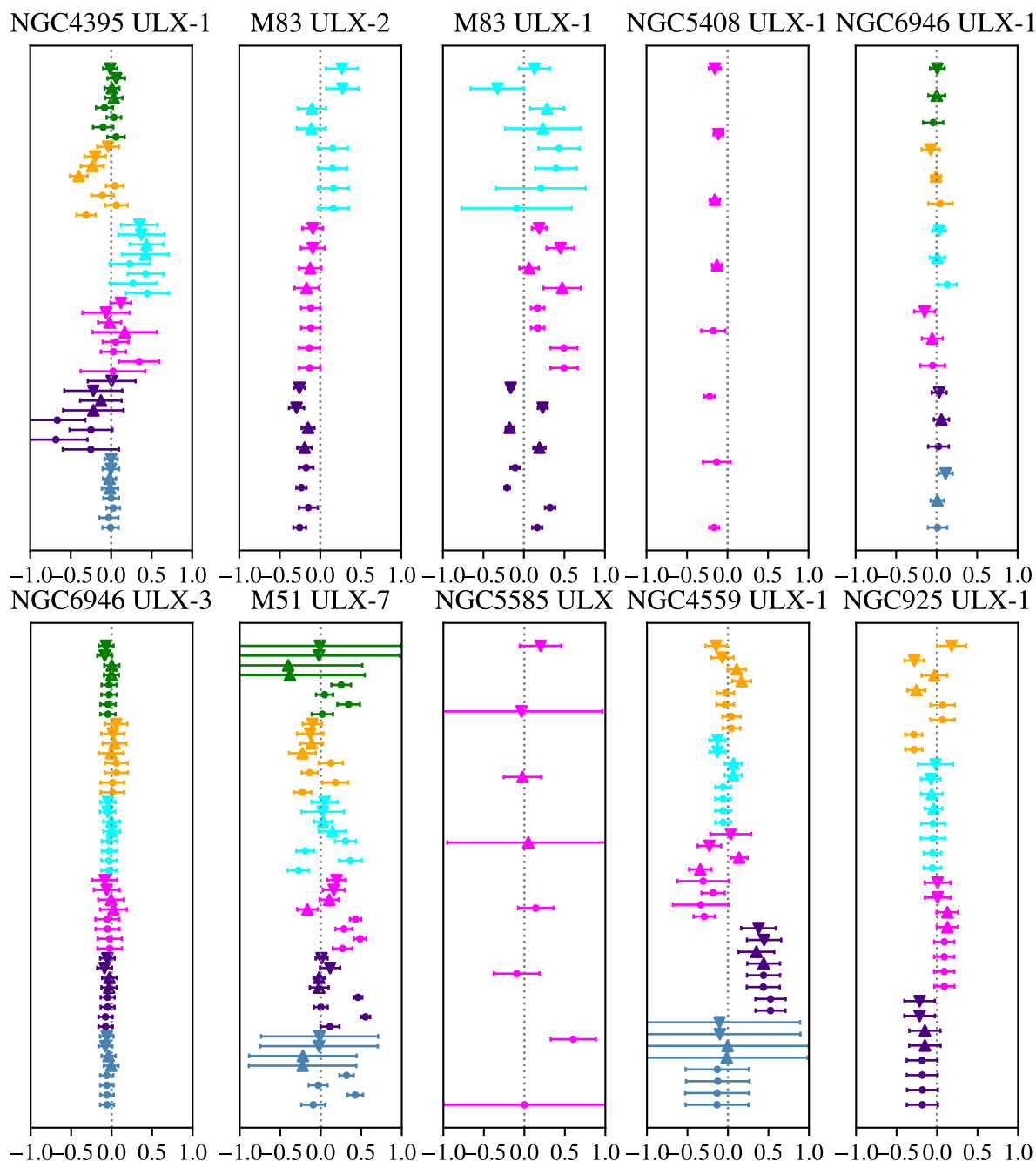


Figure 9. See caption for figure 7.

left to negative. However as we will demonstrate, figure 6 may not encode sufficient information to locate more physical correlations.

Figures 7, 8, 9 and 10 show the correlation coefficient obtained from our simulations for different X-ray bands and UVOT filters. Each errorbar corresponds to a discrete simulation run and is coloured based on the UVOT filter used in the correlation and has a marker corresponding to the XRT band it was correlated against (see caption in figure 7). If the errorbars for a single source consistently deviate far from the dotted line (zero) and are well constrained, then it indicates a consistent correlation between the UVOT filter and the X-ray bands. The sources V404 Cygni, Swift J0243.6+6124, SS433, SMC X-3, NGC300 ULX-1, NGC 7793 P13 and Holmberg IX X-1 show the clearest cases of such correlation. Some errorbars, such as those seen

for the V band in M51 ULX-7, have large sizes due to non-Gaussian distributions for r over the 10,000 Monte-Carlo simulations.

5 DISCUSSION & CONCLUSIONS

Although ULXs are defined empirically by their X-ray luminosity, they are well-known to emit over a broad energy range. Indeed, bright optical/UV emission (in excess of 10^{39} erg s^{-1}) is observed to originate in both Galactic super-critical accretors (SS433: Dolan et al. 1997) and well studied ULXs (NGC 6946 ULX-3: Kaaret et al. 2010) with a mixture of potential origins. In this paper, we have made predictions about how the UV and X-ray emission might correlate

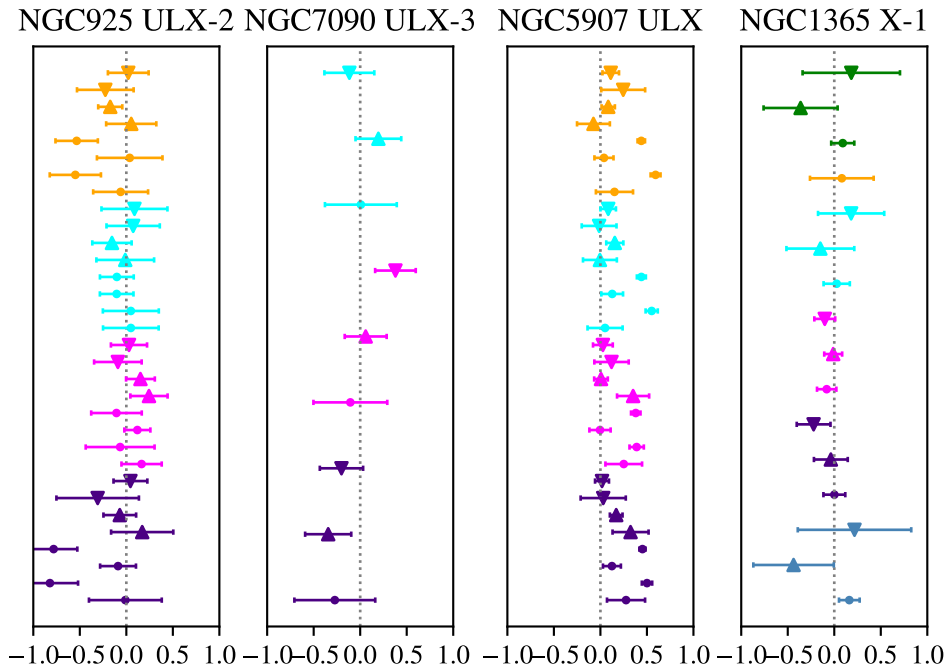


Figure 10. See caption for figure 7.

(or anti-correlate) depending on the dominant mechanism for the low frequency radiation: the irradiated donor star, irradiated outer disc or wind photosphere.

Based on simple arguments, we predict a lack of any correlation between the UV and X-ray emission where the star is irradiated by a wind-cone, as, with the exception of an orientation where the central regions are eclipsed, the X-ray emission should remain constant (in the absence of precession or mass accretion rate changes). In the case of disc irradiation or precession of the super-critical disc/wind, the exact nature of the correlation depends mostly on the observer inclination and any changes in accretion rate at large radius. Certainly for a fixed inclination angle (again, in the absence of precession), a negative correlation would be expected for disc irradiation as the X-ray emission (assumed here to originate within the wind-cone) increases with increasing \dot{m} , but the optical depth to the outer regions also increases. A negative correlation must also result in the case of precession, but can deviate and even become positive when changes in \dot{m} are invoked. In the absence of precession, the emission in both bands is a sensitive function of inclination (see [Poutanen et al. 2007](#); [Middleton et al. 2015a](#)).

NASA’s *Swift* satellite offers an unrivalled opportunity to explore the long timescale changes in both the X-ray and UV bands through simultaneous observing by the XRT and UVOT instruments. For a sample of ~ 40 ULXs, we have extracted the UV and X-ray light curves and searched for correlations, placing constraints on the Pearson coefficient via Monte Carlo simulations.

Our sample contains three Galactic sources, V404 Cygni, Swift J0243.6+6124 and SS433. Strictly speaking, Swift J0243.6+6124, is a ULX under the classical empirical definition, however the other two sources are indirectly identified as supercritical accretors and share many of the same properties of extra-galactic ULXs. V404 Cygni and Swift J0243.6+6124 display among the strongest positive correlations in the sample; the strength of these correlations can be ascribed to large outbursts which subsequently decay over time in both the X-ray and UV/optical bands. The outbursts from both of

these sources have been previously studied (see [Oates et al. 2019](#) and [Liu et al. 2022](#)), however, to our knowledge this is the first time UVOT data has been used in a study for Swift J0243.6+6124. SMC X-3 is another source that displayed an X-ray outburst in 2016 ([Weng et al. 2017](#); [Tsygankov et al. 2017](#); [Townsend et al. 2017](#)); before dimming below the *Swift* detection threshold, many of the observations were taken in windowed timing mode without simultaneous observations in the UV. The combination of the large dynamic range in X-ray count rate and the low number of datapoints may well bias our inferred correlations for this source.

NGC 300 ULX-1 has a bright counterpart and the system has been identified as a ULX pulsar with a supergiant companion ([Carpano et al. 2018](#); [Heida et al. 2019](#)); it is also the closest of the ULXs in our sample to consistently display correlated variability. Initially thought to be supernova due to its transient nature in the optical ([Monard 2010](#)), the source has been studied using the UVOT by ([Villar et al. 2016](#)). We observe that the B band appears to display a negative correlation. From the lightcurves (available in the supplementary material), we observe that the source was bright in the B band around 2010 with count rates peaking at $\sim 10 - 15 \text{ ct s}^{-1}$ and X-ray count rates of $\sim 0.05 \text{ ct s}^{-1}$ (in the full X-ray band). In 2017 the opposite behaviour occurred with X-ray count rates peaking at $\sim 0.12 \text{ ct s}^{-1}$ and B band count rates of $\sim 4 \text{ ct s}^{-1}$.

There are clearly several objects where the correlation between bands is negative. This can result from precession at fixed accretion rate, a changing accretion rate without precession but at viewer inclinations **not** into the wind-cone, or from irradiation of the outer disc for viewer inclinations into the wind-cone. This appears to be the case for NGC 300 ULX-1 and Holmberg IX X-1 (see bottom left figure 6), both of which are systems where precession has been suggested by previous authors ([Weng & Feng 2018](#); [Vasilopoulos et al. 2019](#)). It is also apparent that in some cases, the nature of the correlation changes for a single source between bands (see Holmberg IX X-1 in figure 8. This likely indicates that each band is affected to a differing degree by one of the different processes mentioned above.

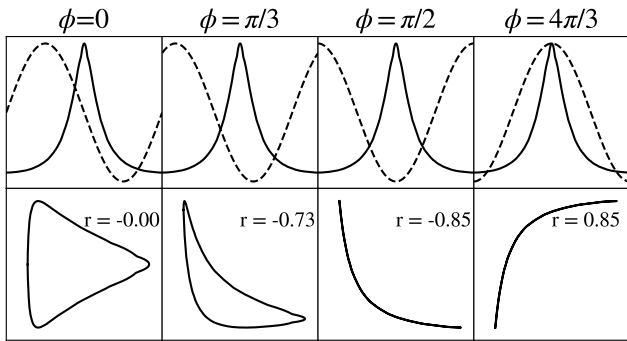


Figure 11. Superimposed light curves with different phases (top row) obtained from the combination of a sigmoid-like light curve (black) from ULXLC, and a sinusoidal profile (dotted) predicted for the UV emission. The bottom row shows the resulting correlation shapes and the associated r value. The parameters for the ULXLC used were $\theta = 5^\circ$, $\Delta i = 9^\circ$ and $i = 15^\circ$ (see Dauser et al. 2017).

In our analysis, we have assumed the simplest case of a linear correlation. However, numerous sources show clear patterns of behaviour where an ‘L’ shape is mapped out (see figure 12), while others show non-linear shapes; a simple linear correlation test (Pearson) is naturally less sensitive to detecting such behaviours. Intriguingly, an ‘L’ shape naturally results from precession of the wind-cone; using ULXLC (Dauser et al. 2017) we create an example X-ray lightcurve using the parameters $\theta = 5^\circ$, $\Delta i = 9^\circ$ and $i = 15^\circ$, which provides a quasi-sigmoid profile (see the first row of figure 11). We assume that the UV/optical profile is sinusoidal (assuming a quasi-spherical geometry of the outer photosphere of the wind), and plot the subsequent profile of the correlation that would result for different phases of precession. In the case of $\phi = 0$, the two curves produce a triangular shape which results in a Pearson correlation coefficient of $r = 0$, which demonstrates that even though the two curves are correlated, the value of r does not reveal this. As the phase is changed to $\pi/2$ the curves produce a characteristic ‘L’ shape which is similar to some of those seen in our light-curves (such as Holmberg IX X-1). This preliminary result may suggest that more complicated (physical) models may be required to understand and search for correlated variability between bands, and that systems which show such ‘L’ shaped correlations, may be our clearest indication of precession.

ACKNOWLEDGEMENTS

NK acknowledges support via STFC studentship project reference: 2115300.

MM is supported by STFC through grant ST/V001000/1.

This work made use of data supplied by the UK Swift Science Data Centre at the University of Leicester.

The authors thank the anonymous referee for useful suggestions.

DATA AVAILABILITY

The data underlying this article are available in the supplementary material (online).

The data includes the XRT and UVOT lightcurves, Source tables with extraction regions, mean count rates and number of observations, the supplementary material also includes the full set of simulation results in this paper.

The source code for this paper may be found at: https://github.com/nx1/anticorr_data/

REFERENCES

- Abazajian K. N., et al., 2009, *ApJS*, **182**, 543
 Bachetti M., et al., 2014, *Nature*, **514**, 202
 Barbon R., Buondi V., Cappellaro E., Turatto M., 2008, VizieR Online Data Catalog.
 Bauer F. E., Brandt W. N., 2004, *ApJ*, **601**, L67
 Bernadich M. C., Schwope A. D., Kovlakas K., Zezas A., Traulsen I., 2022, *A&A*, **659**, A188
 Blundell K. M., Bowler M. G., 2004, *ApJ*, **616**, L159
 Brightman M., et al., 2016, *ApJ*, **816**, 60
 Brightman M., et al., 2018, *Nature Astronomy*, **2**, 312
 Burrows D. N., et al., 2005, *Space Sci. Rev.*, **120**, 165
 Cappellari M., et al., 2011, *MNRAS*, **413**, 813
 Carpano S., Haberl F., Maitra C., Vasilopoulos G., 2018, *MNRAS*, **476**, L45
 Chashkina A., Lipunova G., Abolmasov P., Poutanen J., 2019, *A&A*, **626**, A18
 Cherepashchuk A., 2002, *Space Sci. Rev.*, **102**, 23
 Dai L., McKinney J. C., Roth N., Ramirez-Ruiz E., Miller M. C., 2018, *ApJ*, **859**, L20
 Dauser T., Middleton M., Wilms J., 2017, *MNRAS*, **466**, 2236
 Dolan J. F., et al., 1997, *A&A*, **327**, 648
 Doroshenko V., Tsygankov S., Santangelo A., 2018, *A&A*, **613**, A19
 Earnshaw H. P., Roberts T. P., Middleton M. J., Walton D. J., Mateos S., 2019, *MNRAS*, **483**, 5554
 Evans P. A., et al., 2009, *MNRAS*, **397**, 1177
 Fabrika S., 2004, *APSPR*, **12**, 1
 Feng H., Kaaret P., 2008, *ApJ*, **675**, 1067
 Fürst F., et al., 2016, *ApJ*, **831**, L14
 Fürst F., et al., 2018, *A&A*, **616**, A186
 Fürst F., et al., 2021, *A&A*, **651**, A75
 Fürst F., et al., 2023, *A&A*, **672**, A140
 Gaia Collaboration 2018, VizieR Online Data Catalog, p. I/345
 Gaia Collaboration 2020, VizieR Online Data Catalog, p. I/350
 Gehrels N., et al., 2004, *ApJ*, **611**, 1005
 Gierliński M., Done C., Page K., 2008, *MNRAS*, **388**, 753
 Heida M., et al., 2014, *MNRAS*, **442**, 1054
 Heida M., et al., 2019, *ApJ*, **883**, L34
 Israel G. L., et al., 2017, *Science*, **355**, 817
 Jiang Y.-F., Stone J. M., Davis S. W., 2014, *ApJ*, **796**, 106
 Jiang Y.-F., Stone J. M., Davis S. W., 2019, *ApJ*, **880**, 67
 Kaaret P., Simet M. G., Lang C. C., 2006, *ApJ*, **646**, 174
 Kaaret P., Feng H., Wong D. S., Tao L., 2010, *ApJ*, **714**, L167
 Kaaret P., Feng H., Roberts T. P., 2017, *ARA&A*, **55**, 303
 Karachentsev I. D., Kaisina E. I., Kashibadze Nasonova O. G., 2017, *AJ*, **153**, 6
 Kaur A., et al., 2012, *A&A*, **538**, A49
 Khabibullin I., Sazonov S., 2016, *MNRAS*, **457**, 3963
 King A., Lasota J.-P., 2020, *MNRAS*, **494**, 3611
 King A. R., Davies M. B., Ward M. J., Fabbiano G., Elvis M., 2001, *ApJ*, **552**, L109
 King A., Lasota J.-P., Middleton M., 2023, *New Astron. Rev.*, **96**, 101672
 Kosec P., Pinto C., Fabian A. C., Walton D. J., 2018, *MNRAS*, **473**, 5680
 Kosec P., et al., 2021, *MNRAS*, **508**, 3569
 Kovlakas K., Zezas A., Andrews J. J., Basu-Zych A., Fragos T., Hornschemeier A., Lehmer B., Ptak A., 2020, *MNRAS*, **498**, 4790
 Lianou S., Barmby P., Mosenkov A. A., Lehnert M., Karczewski O., 2019, *A&A*, **631**, A38
 Lin D., Webb N. A., Barret D., 2012, *ApJ*, **756**, 27
 Liu J.-F., Bregman J. N., 2005, *ApJS*, **157**, 59
 Liu J.-F., et al., 2015, *Nature*, **528**, 108
 Liu W., et al., 2022, *A&A*, **666**, A110

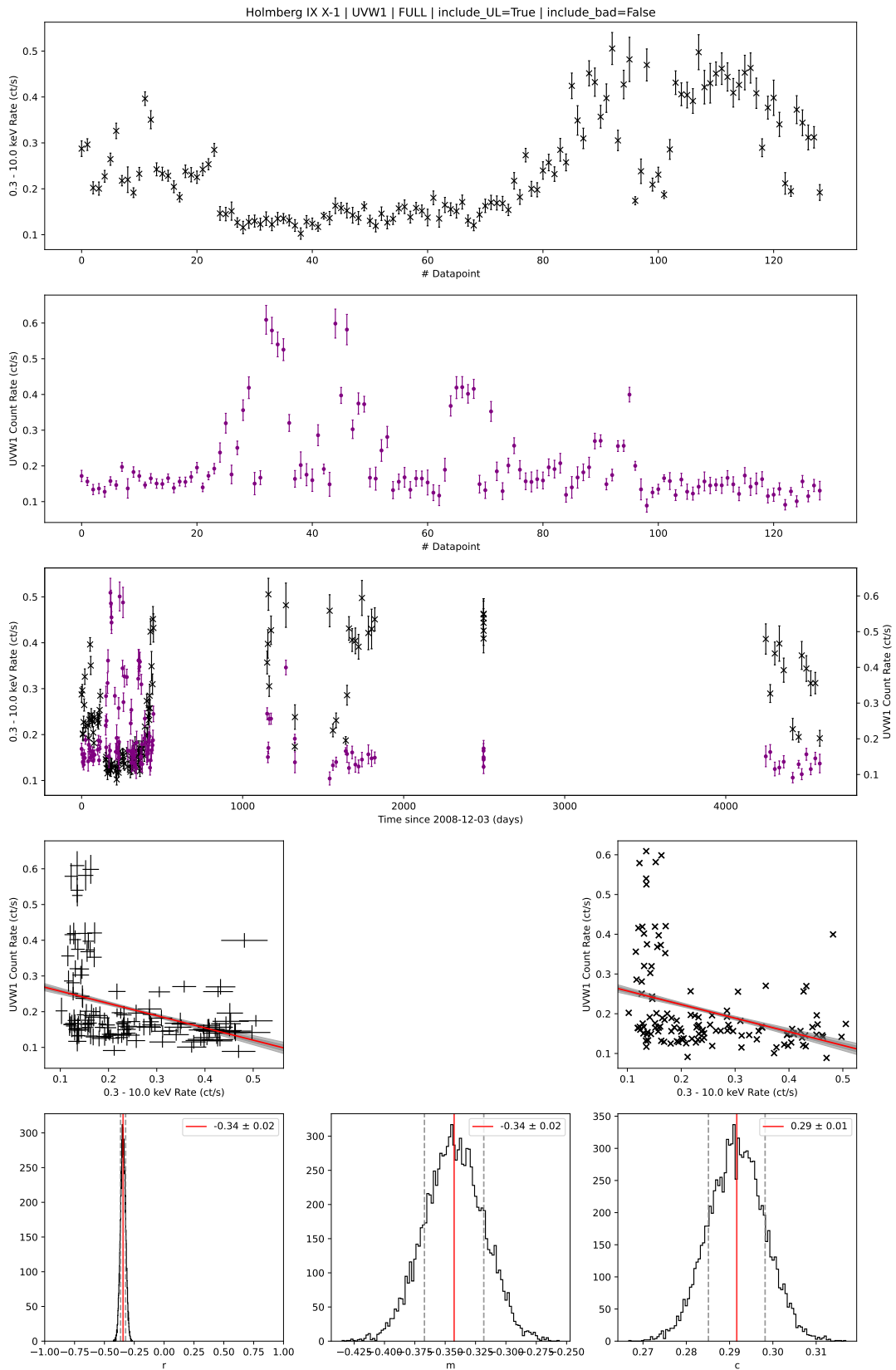


Figure 12. Row 1 & 2: The full band XRT and UVW1 light curves for Holmberg IX X-1 (plotted sequentially) with simultaneous observations. Row 3: The same light curves overlaid. Row 4: The correlated data points, with and without errors, plotted with the best fitting linear model in red (1 and 2σ contours are shaded in grey). Row 5: The distribution of the fit parameters r , m and c for these correlations.

Long K. S., Kuntz K. D., Blair W. P., Godfrey L., Plucinsky P. P., Soria R., Stockdale C., Winkler P. F., 2014, *ApJS*, **212**, 21
 Meurer A., et al., 2017, *PeerJ Computer Science*, **3**, e103
 Middleton M. J., Walton D. J., Roberts T. P., Heil L., 2014, *MNRAS*, **438**, L51
 Middleton M. J., Heil L., Pintore F., Walton D. J., Roberts T. P., 2015a, *MNRAS*, **447**, 3243
 Middleton M. J., Walton D. J., Fabian A., Roberts T. P., Heil L., Pinto C., Anderson G., Sutton A., 2015b, *MNRAS*, **454**, 3134
 Middleton M. J., et al., 2018, *MNRAS*, **475**, 154
 Middleton M. J., Brightman M., Pintore F., Bachetti M., Fabian A. C., Fürst F., Walton D. J., 2019a, *MNRAS*, **486**, 2
 Middleton M. J., Fragile P. C., Ingram A., Roberts T. P., 2019b, *MNRAS*, **489**, 282
 Middleton M. J., et al., 2021, *MNRAS*, **506**, 1045
 Middleton M. J., Higginbottom N., Knigge C., Khan N., Wiktorowicz G., 2022, *MNRAS*, **509**, 1119
 Miller-Jones J. C. A., Jonker P. G., Dhawan V., Brisken W., Rupen M. P., Nelemans G., Gallo E., 2009, *ApJ*, **706**, L230
 Monard L. A. G., 2010, Central Bureau Electronic Telegrams, **2289**, 1
 Motch C., Pakull M. W., Soria R., Grisé F., Pietrzyński G., 2014, *Nature*, **514**, 198
 Motta S. E., et al., 2017, *MNRAS*, **471**, 1797
 Mushtukov A. A., Suleimanov V. F., Tsygankov S. S., Ingram A., 2017, *MNRAS*, **467**, 1202
 Narayan R., Saiğdowski A., Soria R., 2017, *MNRAS*, **469**, 2997
 Oates S. R., et al., 2019, *MNRAS*, **488**, 4843
 Oey M. S., et al., 2007, *ApJ*, **661**, 801
 Pannuti T. G., Schlegel E. M., Filipović M. D., Payne J. L., Petre R., Harrus I. M., Staggs W. D., Lacey C. K., 2011, *AJ*, **142**, 20
 Pasham D. R., Strohmayer T. E., 2013a, *ApJ*, **764**, 93
 Pasham D. R., Strohmayer T. E., 2013b, *ApJ*, **774**, L16
 Pinto C., Middleton M. J., Fabian A. C., 2016, *Nature*, **533**, 64
 Pinto C., et al., 2017, *MNRAS*, **468**, 2865
 Poutanen J., Lipunova G., Fabrika S., Butkevich A. G., Abolmasov P., 2007, *MNRAS*, **377**, 1187
 Pringle J. E., 1996, *MNRAS*, **281**, 357
 Roberts T. P., 2007, *Ap&SS*, **311**, 203
 Rodríguez Castillo G. A., et al., 2020, *ApJ*, **895**, 60
 Roming P. W. A., et al., 2005, *Space Sci. Rev.*, **120**, 95
 Sathyaprakash R., et al., 2019, *MNRAS*, **488**, L35
 Shakura N. I., Sunyaev R. A., 1973, *A&A*, **500**, 33
 Shimura T., Takahara F., 1995, *ApJ*, **445**, 780
 Strateva I. V., Komossa S., 2009, *ApJ*, **692**, 443
 Sutton A. D., Roberts T. P., Middleton M. J., 2013, *MNRAS*, **435**, 1758
 Swartz D. A., Ghosh K. K., Tennant A. F., Wu K., 2004, *ApJS*, **154**, 519
 Swartz D. A., Soria R., Tennant A. F., Yukita M., 2011, *ApJ*, **741**, 49
 Townsend L. J., Kennea J. A., Coe M. J., McBride V. A., Buckley D. A. H., Evans P. A., Udalski A., 2017, *MNRAS*, **471**, 3878
 Tsygankov S. S., Doroshenko V., Lutovinov A. A., Mushtukov A. A., Poutanen J., 2017, *A&A*, **605**, A39
 Tully R. B., Courtois H. M., Sorce J. G., 2016, *AJ*, **152**, 50
 Vasilopoulos G., Petropoulou M., Koliopoulos F., Ray P. S., Bailyn C. B., Haberl F., Gendreau K., 2019, *MNRAS*, **488**, 5225
 Vasilopoulos G., Lander S. K., Koliopoulos F., Bailyn C. D., 2020, *MNRAS*, **491**, 4949
 Villar V. A., et al., 2016, *ApJ*, **830**, 11
 Vinokurov A., Atapin K., Solovyeva Y., 2020, *ApJ*, **893**, L28
 Walton D. J., et al., 2016, *ApJ*, **826**, L26
 Walton D. J., et al., 2018a, *MNRAS*, **473**, 4360
 Walton D. J., et al., 2018b, *ApJ*, **857**, L3
 Walton D. J., Mackenzie A. D. A., Gully H., Patel N. R., Roberts T. P., Earnshaw H. P., Mateos S., 2022, *MNRAS*, **509**, 1587
 Webb N. A., Barret D., Godet O., Servillat M., Farrell S. A., Oates S. R., 2010, *ApJ*, **712**, L107
 Weng S.-S., Feng H., 2018, *ApJ*, **853**, 115
 Weng S.-S., Ge M.-Y., Zhao H.-H., Wang W., Zhang S.-N., Bian W.-H., Yuan Q.-R., 2017, *ApJ*, **843**, 69

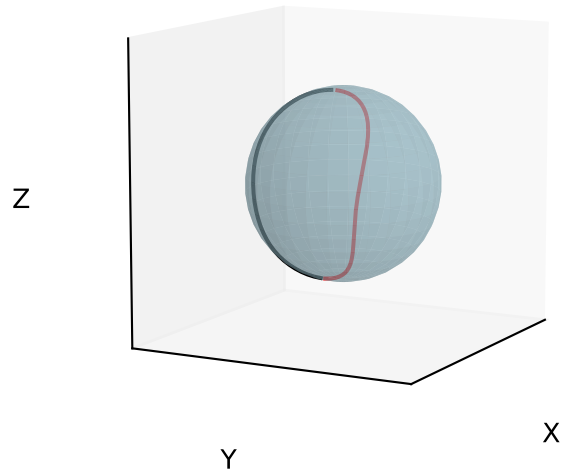


Figure A1. The intersection of a cone with opening angle $\theta = 15^\circ$ and a star at position $x_0 = 2$, $y_0 = 0$, $z_0 = 10$ and a radius of $r = 2.2$. These set of parameters make it such that the cone is grazing the star. This figure is an intermediate step in our calculations where we have yet to cull the path due to obscuration of the star itself.

van den Eijnden J., et al., 2020, *MNRAS*, **496**, 4127

APPENDIX A: IRRADIATED COMPANION MODEL

We model a cone of emission centred at the origin $(0, 0, 0)$ with opening parameter $c = \sin(\theta/2)$ where θ is the full opening angle of the cone. We then place a companion star, modelled as a sphere placed at (x_0, y_0, z_0) with radius r .

The equations and the cone and sphere in Cartesian coordinates are given by equations A1 and A2 respectively, this geometry allows us to define the z axis as being in-line with the radiation of the beamed cone of emission and adjust the position of the star relative to this axis.

$$\frac{x^2 + y^2}{c^2} = z^2 \quad (\text{A1})$$

$$(x - x_0)^2 + (y - y_0)^2 + (z - z_0)^2 = r^2 \quad (\text{A2})$$

We then solve A1 and A2 simultaneously for x , y using the SymPy Python package (Meurer et al. 2017), this provides four solutions, positive and negative for both $x(z)$ and $y(z)$.

These equations allow us to calculate the x and y coordinates for a given z that corresponds intersection between the cone of emission and the sphere, by ignoring the z coordinate and plotting only the x and y values, we may obtain the projection that would be observed by an observer situated down the line-of-sight of the z axis. Since the cone is centred at the origin, by applying a rotation $R_x(i)$ or $R_y(i)$ and re-projecting down the z axis, we can simulate the effect of an observation at a specified inclination (with respect to the jet axis).

We then cut any values of the intersection that are above the hemisphere of the star ($z > z_0$) as these parts would not be illuminated by the beam. If the configuration is such that the star passes through one wall of the cone as seen in figure A1, then we consider this as an

edge case and explicitly calculate the new path by joining the culled path with the arc created from the circle bounded by the hemisphere of the star.

The result is a closed path, defined by x, y coordinates of the area that would be seen by an observer, the area is calculated via two methods, one using the shoelace formula and the other via triangulation both of consistently produce the same result.

This paper has been typeset from a \TeX/L\AA\TeX file prepared by the author.